

Fatigue Behavior of Solid-State Additive Manufactured Inconel 625

D.Z. AVERY,¹ O.G. RIVERA,¹ C.J.T. MASON,¹ B.J. PHILLIPS,¹
J.B. JORDON ^{1,3} J. SU,² N. HARDWICK,² and P.G. ALLISON¹

1.—Department of Mechanical Engineering, The University of Alabama, Tuscaloosa, AL 35487, USA. 2.—MELD Manufacturing Corporation, Christiansburg, VA 24703, USA. 3.—e-mail: bjordan@eng.ua.edu

A transformative hybrid solid-state additive manufacturing process provides a new path to fabricate or repair components with wrought-like performance. In this work, the fatigue behavior of Inconel 625 (IN625) manufactured via a high-shear deposition process is quantified for the first time. In this unique process, feedstock is deposited via a hollow non-consumable rotating cylindrical tool, thereby generating heat and plastically deforming the feedstock through controlled pressure as consecutive layers are metallurgically bonded upon a substrate. To quantify the fatigue behavior of the as-deposited IN625, stress-life experiments were conducted, where improved fatigue resistance was observed compared with the feedstock. Post-mortem analysis of the as-deposited IN625 revealed a similar fatigue nucleation and growth mechanism to the feedstock for a majority of the specimens tested in this study. Last, a microstructure-sensitive fatigue life model was utilized to elucidate structure-property fatigue mechanism relations of the as-deposited and feedstock IN625 materials.

INTRODUCTION

The need for additively manufactured metal alloys has grown exponentially in recent years because of limitations of traditional manufacturing processes in fabrication of complex parts.¹ This growth has led to a variety of additive manufacturing technologies, including electron beam melting (EBM),^{2,3} selective laser melting (SLM),^{1,2,4} laser consolidation (LC),⁵ direct metal deposition (DMD),^{6,7} and friction stir weld additive manufacturing (FSWAM).^{8,9} A common additive material used in DMD and SLM is Inconel 625 (IN625).^{5,10–13} IN625 is a nickel-based superalloy, strengthened by precipitation of carbides, γ' , and γ'' ,^{14,15} that exhibits high strength and ductility at elevated temperatures.^{10,14–17} In addition, IN625 exhibits good low cycle fatigue resistance at elevated temperatures.^{21,22}

Fusion-based additive manufacturing (AM) processes, e.g., SLM and EBM, require melting of IN625 to metallurgically bond successive deposited layers together. The solidification of IN625 typically increases the void volume fraction and produces

columnar or dendritic grain morphology that usually has a deleterious effect on mechanical properties. In particular, the fatigue properties of LC and SLM show a significant decrease in fatigue resistance compared with wrought IN625.^{4,5} As such, a novel AM process that uses high-shear deformation to achieve solid-state depositions¹⁸ can produce fully-dense, near-net shape IN625 AM components from solid or powder feedstock. Previous research has shown that this process, commercially known as MELD, can produce a refined microstructure resulting in higher mechanical properties compared with other fusion-based processes.^{18,19}

To the best of the authors' knowledge, this work is the first to quantify the fatigue behavior of the high-shear solid-state deposition process. In this article, stress-controlled fatigue experiments were carried out to compare as-deposited and wrought feedstock IN625 specimens. In addition, microstructural characterization and post-mortem analysis of fractured surfaces was performed on the as-deposited and feedstock specimens to elucidate fatigue mechanisms. Last, a high-fidelity microstructure-dependent fatigue life model was implemented to relate

the fatigue behavior based on the experimental stress-life and microstructural characterization results generated in this study.

MATERIALS AND METHODS

The feedstock material used in the study was an extruded hot rolled and annealed ATI IN625. The high-shear solid-state deposition of IN625 was manufactured by MELD Manufacturing Corp. using the MELD process by extruding a solid IN625 feedstock rod through a hollow tool onto a HY80 substrate, as shown in Fig. 1. The MELD process creates solid-state depositions by plastically deforming the feedstock onto a substrate by a combination of hydrostatic pressure and frictional heat generated by the tool shoulder, which in turn produces a metallurgical bond between deposited layers. For this study, five successive layers of IN625 depositions were made using the MELD process, where the build height for each layer was 0.5 mm.

As-deposited and feedstock specimens were mounted in respective loading directions in conductive media and then ground with 1200 grit SiC paper and polished down to $1\ \mu\text{m}$ with diamond suspension. The as-deposited and feedstock initial-state microstructures were quantified using optical micrographs coupled with imaging post-processing software. A scanning electron microscope (SEM), Tescan Lyra FIB-FESEM, coupled with an EDAX Hikari Super Electron Backscatter Diffraction (EBSD) camera was used to perform Euler EBSD texture mapping and post-mortem analysis.

Due to the limited volume of material provided by the manufacturer, this research employed a subscaled hourglass fatigue specimen in the study as shown in Fig. 1c. The fatigue specimen is a modified

design similar to Rettberg et al.²⁰ The fatigue specimens were machined using wire electrical discharge machining (EDM) in the long traverse loading direction for as-deposited IN625 specimens, where the feedstock specimens were oriented in the extruded direction. Due to limited size of sub-sized fatigue specimens, the surface finish for both feedstock and as-deposited IN625 was left as machined for direct comparison. Stress-control fatigue experiments were conducted using an MTS servo hydraulic load frame equipped with a 20-kN load cell. Specimens were tested at $R = 0.1$ in ambient temperature and relative humidity (50%) until fracture. Upon fracture, the specimen fracture surfaces were mounted for SEM fractography analysis to determine crack initiation and crack propagation characteristics.

The Microstructure-Sensitive Fatigue Model

The microstructure-sensitive fatigue model (MSF) implemented in this study was first proposed by McDowell^{21,22} for cast aluminum alloy A356-T6.²³ The model was further expanded to additional aluminum alloys,^{24–27} other material systems,^{28–34} and AM processes.^{35,36} This study provides an additional investigation into the development of the MSF model to include a nickel-based superalloy, IN625, and to model the fatigue resistance of high-shear deposited IN625. Microstructure features and mechanical properties specifically related to the as-deposited IN625 were used to model the as-deposited IN625 fatigue behavior.

The high-fidelity fatigue model is based on three distinct and experimentally observed stages of fatigue damage:

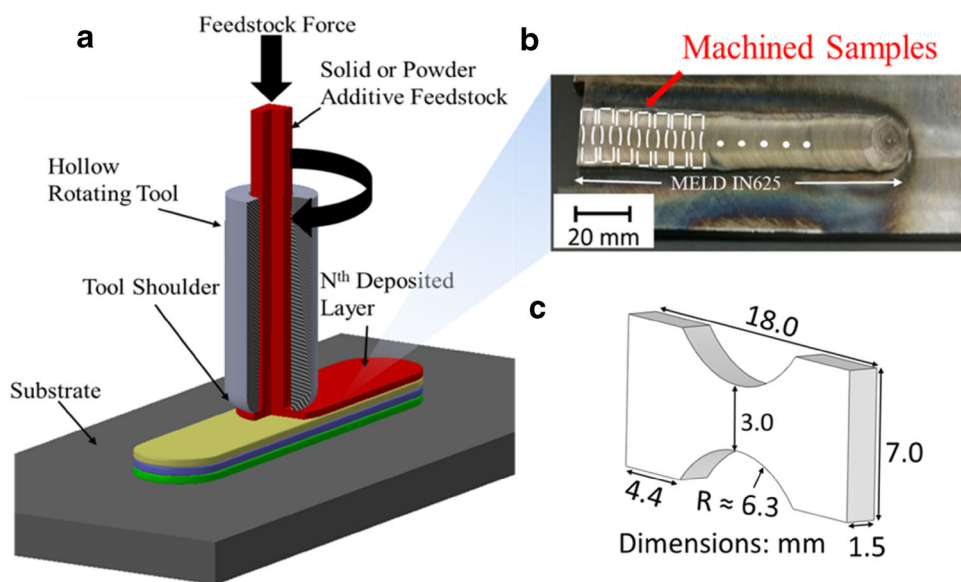


Fig. 1. (a) Schematic of the MELD process with a solid rod extruded through the hollow stirring tool. (b) As-deposited IN625 sample on a HY80 substrate. (c) Fatigue specimen geometry used for both as-deposited IN625 and feedstock IN625 specimens.

$$N_{\text{Total}} = N_{\text{Inc}} + N_{\text{MSC/PSC}} + N_{\text{LC}} \quad (1)$$

where N_{Total} denotes the total number of cycles to failure, N_{inc} represents the number of cycles to develop a crack, $N_{\text{MSC/PSC}}$ characterizes the number of cycles to propagate in the microstructurally small (MSC) and physically small crack (PSC) growth regime, and N_{LC} is the number of cycles for the long crack (LC) stage.

A modified Coffin–Manson law is employed to calculate the cycles till incubation of a crack, N_{inc} , by modeling the nonlocal microscale damage associated with incubation around an inclusion. This parameter is expressed by β , where this material variable is associated with material inclusions and is expressed by Eq. 2.

$$C_{\text{inc}} N_{\text{inc}}^z = \beta = \frac{\Delta\gamma_{\text{max}}^{p*}}{2} \quad (2)$$

$$C_{\text{inc}} = \text{CNC} + z(C_m - \text{CNC}) \quad (3)$$

$$\text{CNC} = C_n(1 - R) \quad (4)$$

where C_{inc} and α are linear and exponential coefficients for the modified Coffin–Manson law for crack incubation obtained by estimating the number of cycles for incubation life [Eq. 2]. Furthermore, C_m and C_n are model constants, R is the load ratio (i.e., $R = 0.1$), and z is the localization multiplier. The localization parameter is greater than zero above the microplasticity fatigue damage percolation threshold and as plastic shear strain increases the localization multiplier shifts to unity [Eq. 5]. Additionally, β is related to the maximum local plastic shear strain amplitude at an inclusion, $\frac{\Delta\gamma_{\text{max}}^{p*}}{2}$, and is expressed in Eqs. 6 and 7.

$$z = \frac{\frac{1}{D} - \eta_{\text{lim}}}{1 - \eta_{\text{lim}}} \quad (5)$$

$$\beta = \frac{\Delta\gamma_{\text{max}}^{p*}}{2} = Y[\varepsilon_a - \varepsilon_{\text{th}}]^q, \frac{l}{D} < \eta_{\text{lim}} \quad (6)$$

$$\beta = \frac{\Delta\gamma_{\text{max}}^{p*}}{2} = Y(1 + \zeta z)[\varepsilon_a - \varepsilon_{\text{th}}]^q, \frac{l}{D} > \eta_{\text{lim}} \quad (7)$$

where the critical inclusion size that incubates a crack is denoted as D , the length of the microplasticity zone in front of an inclusion is represented by l , and the limiting factor that defines the transition from constrained to unconstrained micronotch root plasticity and is governed by the ratio of the plastic zone size to the inclusion size with respect to the applied strain amplitude is η_{lim} . Additionally, ε_a is the remote applied strain amplitude and ε_{th} is the microplasticity threshold. The ratio $\frac{l}{D}$ is defined as the square root of the ratio of the plastic zone over the inclusion area and is expressed in Eqs. 8 and 9 for constrained and unconstrained micronotch root plasticity, respectively. The parameters q and ζ are determined from micromechanical simulations.³⁷

The parameter Y ³⁷ is correlated as $Y = y_1 + 0.1(1 + R)y_2$ where y_1 and y_2 are model constants. For completely reversed loading cases, $Y = y_1$. The cyclic plastic zone size is calculated using the nonlocal plastic shear strain with respect to the remote loading strain amplitude.³⁷

$$\frac{l}{D} = \eta_{\text{lim}} \frac{(\varepsilon_a - \varepsilon_{\text{th}})}{\varepsilon_{\text{per}} - \varepsilon_{\text{th}}}, \frac{l}{D} \leq \eta_{\text{lim}} \quad (8)$$

$$\frac{l}{D} = 1 - (1 - \eta_{\text{lim}}) \left(\frac{\varepsilon_{\text{per}}}{\varepsilon_a} \right)^r, \frac{l}{D} > \eta_{\text{lim}} \quad (9)$$

where r is the shape constant for the evolution to partial microplasticity.^{38,39} Through micromechanical simulations, the microplasticity constants ε_{th} and ε_{per} , representing the strain threshold and percolation limits, respectively, were established. The microplasticity threshold is represented as a fatigue damage limit, estimated based on the ultimate tensile strength of the material. The percolation limit is the threshold where the cyclic plastic zone increases non-linearly and is estimated as a percentage of the cyclic yield stress. Using the standard endurance limit calculations, $\varepsilon_{\text{th}} = \frac{0.29S_{\text{ut}}}{E}$ and $\varepsilon_{\text{per}} = \frac{0.7\sigma_{\text{cyclic}}}{E}$, the two values can also be calculated. The fatigue crack transitions into the next phase of fatigue damage when the localized plastic zone has been saturated.

The $N_{\text{MSC/PSC}}$ regime is modeled by the crack tip opening displacement and is expressed as:

$$\left(\frac{da}{dN} \right)_{\text{MSC/PSC}} = \chi(\Delta\text{CTD} - \Delta\text{CTD}_{\text{th}}), \quad a_i = 0.625D \quad (10)$$

Here, $\Delta\text{CTD}_{\text{th}}$ is the crack tip displacement threshold, ΔCTD is the crack tip opening displacement range, χ is a constant for a given microstructure, and a_i is the initial crack length as a function of inclusion size. The crack tip opening displacement threshold is estimated to be equivalent to the Burger's vector for the nickel-rich matrix,^{40,41} $\Delta\text{CTD}_{\text{th}} = 2.48 \times 10^{-4} \mu\text{m}$. The crack tip opening displacement range, ΔCTD , is evaluated using Eq. 11.

$$\Delta\text{CTD} = C_{\text{II}} \left(\frac{\text{GS}}{\text{GS}_0} \right)^\omega \left(\frac{\text{GO}}{\text{GO}_0} \right)^\varpi \left[\frac{U\Delta\hat{\sigma}}{S_{\text{ut}}} \right]^\zeta a_i + C_{\text{I}} \left(\frac{\text{GS}}{\text{GS}_0} \right)^\omega \left(\frac{\text{GO}}{\text{GO}_0} \right)^\varpi \left(\frac{\Delta\gamma_{\text{max}}^p}{2} \right)^2 \quad (11)$$

where C_{I} represents the low cycle fatigue material coefficient, and C_{II} and ζ denote the material coefficients and exponents for the high cycle fatigue regime. S_{ut} is the monotonic ultimate tensile strength determined uniaxial tensile tests, and a_i is the initial crack length. GS , GS_0 , GO , GO_0 , ω , and ϖ are grain size and orientation modeling constants. The equivalent uniaxial stress amplitude,

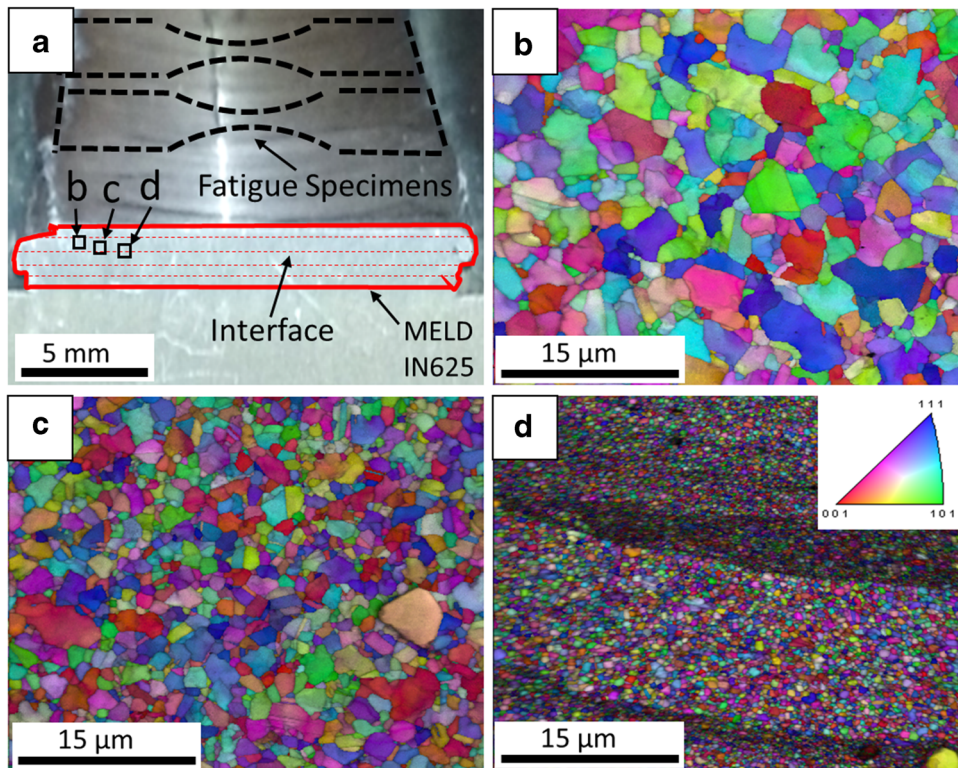


Fig. 2. (a) Schematic of EBSD locations of the high-shear solid-state deposition process. (b) Euler EBSD map representative of the center location of deposited layer with average grain size of $1.2 \mu\text{m}$. (c) EBSD map between the center of the build layer and interface with average grain size of $0.82 \mu\text{m}$. (d) EBSD map of the layer interface of two deposited layers with average grain size of $0.26 \mu\text{m}$.

$\Delta\hat{\sigma} = 2\theta\bar{\sigma}_a + (1d\theta)\Delta\sigma_1$, is defined as the linear combination of effective stress amplitude, $\bar{\sigma}_a = \sqrt{\frac{3}{2} \frac{\Delta\sigma'_y}{2} \frac{\Delta\sigma'_y}{2}}$, and the maximum principal stress range, $\Delta\sigma_1$. The coefficient U is used to model the mean stress effects pertaining to crack growth, where $U = \frac{1}{1-R}$ is for the case when $R \leq 0$ and $U = 1$ for $R > 0$. For this study, the MSF modeling parameters including the local shear damage parameter and small crack growth constants were estimated from our MSF database. Future MSF modeling of the MELD processed IN625 will focus on replica experiments to validate the INC and MSC model parameters initially determined in this study.

The high-fidelity fatigue model includes an LC growth stage that is captured using traditional linear elastic fracture mechanics (LEFM) and is extensively described by Xue et al.³⁷ The LC growth model is utilized for when the fatigue crack approaches several millimeters in length. Thus, the MSF LC growth regime is used for specimens and components with large cross sections. Therefore, this presented work did not model the LC growth regime because of the small fatigue specimen size. The primary focus of this study was to model the number of cycles to incubate a crack, N_{Inc} , and model the number of cycles to grow a crack in the microstructure and small crack regime, $N_{\text{MSC/PSC}}$, similar to previous work.^{26,28,31,33}

RESULTS AND DISCUSSION

Figure 2 displays the Euler EBSD texture maps for three locations of a representative deposited build layer, with average grain size and number of grains. Texture characterization of the representative specimen revealed a significant decrease in the average grain size, from $30 \mu\text{m}$ for the feedstock to $1 \mu\text{m}$ for the as-deposited IN625 material. The area of most significant reduction in grain size occurred at the deposition interface layer, where the grain size reduced to as low as $0.26 \mu\text{m}$ in the interfacial layer of as-deposited IN625, as seen in Fig. 2d. The refined grain size is a product of the depositional process due to dynamic recrystallization of the grains and is supported by the equiaxed grain morphology of as-deposited IN625 material.¹⁸

Figure 3 displays the optical micrographs, where carbides M_{23}C_6 and M_6C ¹⁵ are seen distributed on the polished surface of the feedstock and as-deposited IN625 samples. Figure 3a shows the carbide size and distribution within the feedstock in the mechanical loading orientation. The feedstock loading direction is characterized by large, unevenly dispersed asymmetrical carbides. Figure 3b reveals that the MELD process produced microstructures with small, evenly distributed carbides. Figure 3c shows the normal distribution of carbides based on size, where the high-shear solid-state deposition

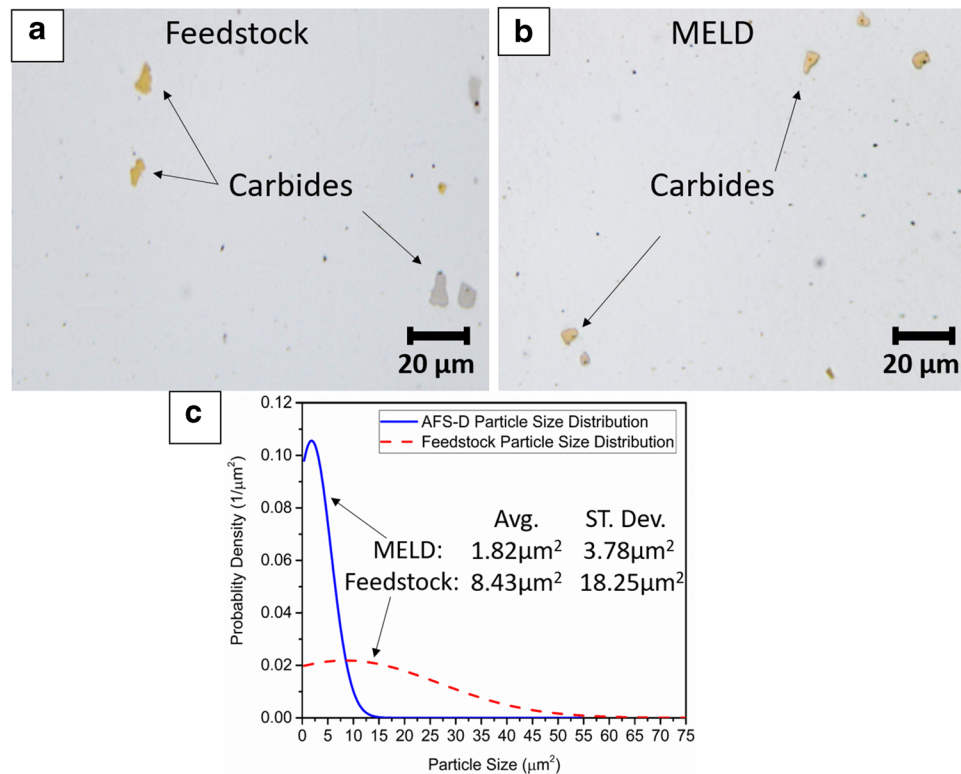


Fig. 3. (a) Optical micrograph of feedstock IN625 constituent particles in loading direction. (b) Optical analysis of constituent particles in as-deposited IN625 material in loading direction. (c) Particle size distribution of as-deposited IN625 and feedstock.

process showed an increase in the carbide density at smaller particle sizes compared with the wrought feedstock. Analysis revealed a decrease of average carbide size ($8.43\text{--}1.82\ \mu\text{m}^2$) and volume fraction (0.773 to 0.437), which suggests that the high-shear solid-state deposition process breaks up the carbides into smaller sub-particles. The lower average carbide size and a smaller nearest neighbor distance of particles ($14.0\text{--}12.0\ \mu\text{m}$) are indicative of a more homogeneous microstructure because of the mechanical processing of the solid-state process.

Representative TEM STEM-HAADF micrographs of feedstock IN625 and as-deposited IN625 are presented in Fig. 4. For comparative purposes, Fig. 4a depicts a STEM-HAADF image of the feedstock microstructure in the loading orientation. Figure 4a exhibits a coarse microstructure with large grains and unevenly distributed carbides within the nickel matrix of the IN625. Figure 4b is a magnified view of an asymmetrical carbide pinned between grain boundaries found in the IN625 feedstock. The large, irregularly shaped carbides of the feedstock correlate well with the size and shape distribution seen in Fig. 3.

Figure 4c shows a STEM-HAADF micrograph of the as-deposited IN625 in the loading direction, which is taken from the interface layer of the high-shear deposition represented by the Euler EBSD map in Fig. 2d. Additionally, Fig. 4d shows the magnified TEM image of a sub-micron grain with a

dispersion of small refined carbides found within the as-deposited IN625. TEM analysis of the feedstock and as-deposited IN625 revealed ultra-fine-grain refinement of the microstructure due to dynamic recrystallization caused by the combination of the hydrostatic pressure and severe plastic deformation of the feedstock during deposition. The TEM analysis correlates the sub-micron grain refinement, found within the interface layer, with the Euler EBSD maps presented in Fig. 2d. The STEM images suggest that severe plastic deformation refined the larger carbides within the feedstock into smaller, more homogeneously dispersed particles within the as-deposited IN625. Figure 4d shows nano-scale particles in the as-deposited IN625, further supporting that the high-shear deposition process can refine the brittle inclusions.

Figure 5 shows the experimental results of the stress-controlled fatigue tests of the as-deposited IN625 and the corresponding feedstock material. Also, shown in Fig. 5 for comparison purposes are experimental stress-life fatigue results of cast and additive laser consolidation (LC) IN625 materials.⁵ As seen in Fig. 5, the as-deposited IN625 exhibited generally greater fatigue resistance compared to feedstock, cast, and LC IN625 materials. In fact, in some load levels, the as-deposited IN625 exhibited upwards of four times the number of cycles to failure compared with the feedstock. This improvement in the mean fatigue behavior of as-deposited

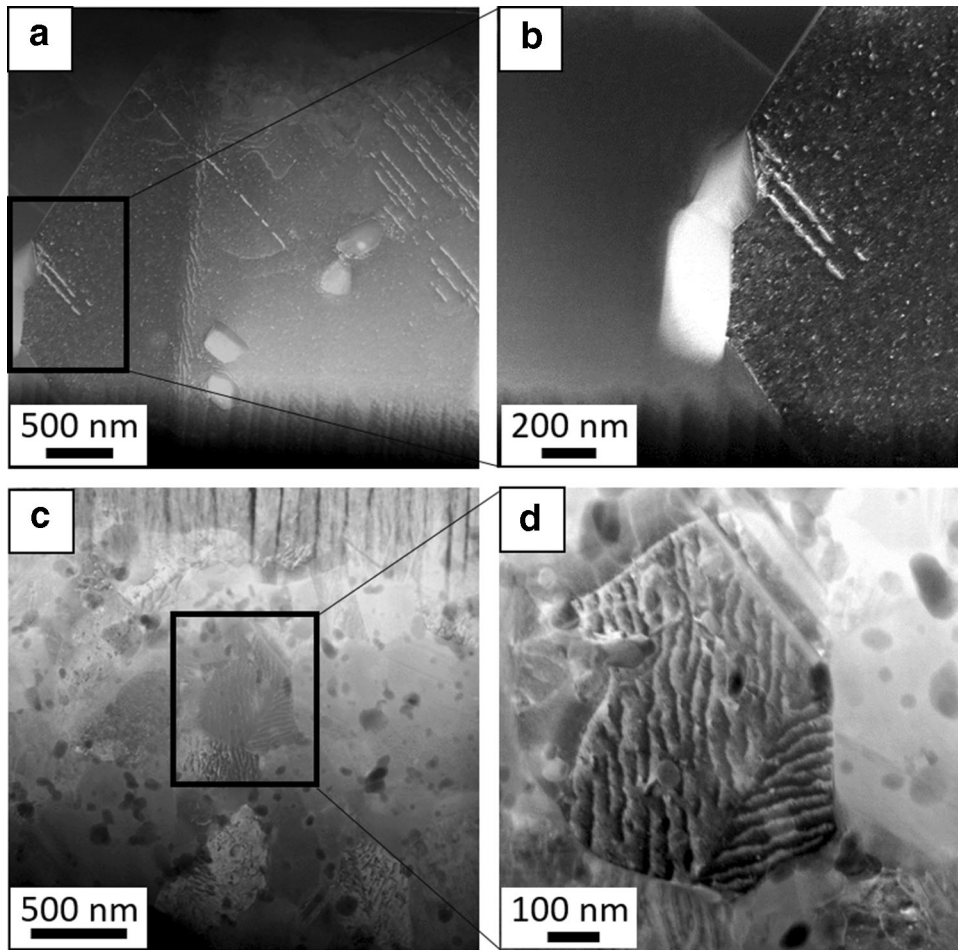


Fig. 4. (a) TEM micrograph of IN625 feedstock exhibiting large grains and carbides taken in loading direction. (b) Magnified view of carbide in feedstock. (c) TEM micrograph of as-deposited IN625 taken from the interface layer in loading direction. (d) Magnified view of as-deposited IN625 refined microstructure with ultra-refined grains and carbides.

IN625 is attributed to the refined microstructure and reduced carbide size and volume fraction produced by the high-shear solid-state deposition process. However, it is important to note that the fatigue behavior of as-deposited IN625 exhibited scatter in the number of cycles to failure, where two specimens in particular tested at 225 MPa and 258.75 MPa stress amplitude failed at 129,974 and 160,734 cycles, respectively. The specimen tested at 225 MPa (A11) that failed at 129,974 cycles was lower than any of the feedstock tested at this stress level. Further discussion of the premature failure of these specimens is presented later in conjunction with the fractography results.

For reference purposes, Fig. 6a shows a representative macroscale fracture surface of a feedstock IN625 specimen, F10, tested at a stress amplitude of 225 MPa that failed at 617,004 cycles. Figure 6b is a magnified view of the crack initiation site where a fractured particle approximately 10 μm in diameter was found to have initiated the fatigue crack. In addition, brittle, irregularly shaped carbides were observed cracked and debonded from the nickel

matrix, creating stress risers that can reduce expected fatigue life of the material as shown in Fig. 6c.

Figure 6d shows a representative fracture surface for the as-deposited IN625 material. This specimen, Specimen A12, was fatigue tested at a stress amplitude of 225 MPa and failed at 983,086 cycles. Figure 6e highlights a typical wrought-like fracture surface that contained river marks pointing to the initiation site. Figure 6f shows a higher magnification of the initiation site, where the fatigue crack grew radially outward from the surface and through the sub-micron layer interface. The as-deposited Specimen A12 fatigue tested at a stress amplitude 225 MPa exhibited a nearly 50% increase in fatigue life compared with feedstock. The improvement in fatigue life is largely attributed to the refined microstructure including reduced grain and carbide size.

Conversely, Fig. 7 depicts the fracture surfaces of the two outliers of the as-deposited IN625 specimens (Specimens A11 and A8). Figure 7a shows the fracture surface of specimen A11 that was fatigue

tested at a stress amplitude of 225 MPa and failed at 129,974 cycles. Figure 7c shows that specimen A8 was fatigue tested at a stress amplitude of 259 MPa that failed at 160,734 cycles. Based on the post-mortem SEM analysis, delamination cracks were observed at the location of the fatigue crack initiation sites of both as-deposited specimens, as shown Fig. 6b, d. As such, interlayer delamination of the as-deposited specimens appeared to decrease the number of cycles required to nucleate the fatigue crack, thus increasing the scatter of the fatigue results of the as-deposited material, as shown in Fig. 5. We acknowledge that it is unclear if the high microstructure gradient at the interface layer

causes a crack to incubate or if it is due to non-uniform metallurgical bonding of the interface layer. Our prior investigation of the microstructure reported elsewhere¹⁸ did not reveal any significant variation between sample locations or layers. Thus, it is not clear why a few samples experienced crack incubation at the interface layer, thus resulting in underperformance, while the majority of the samples showed no crack incubation caused by delamination. Future work will focus on addressing the issue of crack incubation at the interlayer.

Figure 8a displays the striation spacing for the feedstock specimen F10 and the as-deposited IN625 specimen A12. During striation analysis, characteristic river marks were observed flowing radially outward from crack initiation sites for both fatigue specimens. Each crack grew outward from either a cracked particle (Fig. 6b) or the surface (Fig. 6e) toward the specimen center. Over several striations, Fig. 8a displays the average striation spacing. Both specimens exhibited scatter of the measured striations, which are caused by non-uniform microstructural features such as grains and particles sizes that vary within the material. This variation of constituent particles and microstructure provides disparity with striation spacing in a fatigue specimen. The striation spacing of feedstock specimen F10 became non-linear at approximately 600–800 μm from the crack initiation site. However, the striation spacing of the as-deposited specimen A12 became non-linear at approximately 900–1100 μm from the crack initiation site. Additionally, seen in Fig. 8a, the final crack length before the transition into fast fracture for the feedstock is approximately 1200 μm, while for the as-deposited specimen the final crack

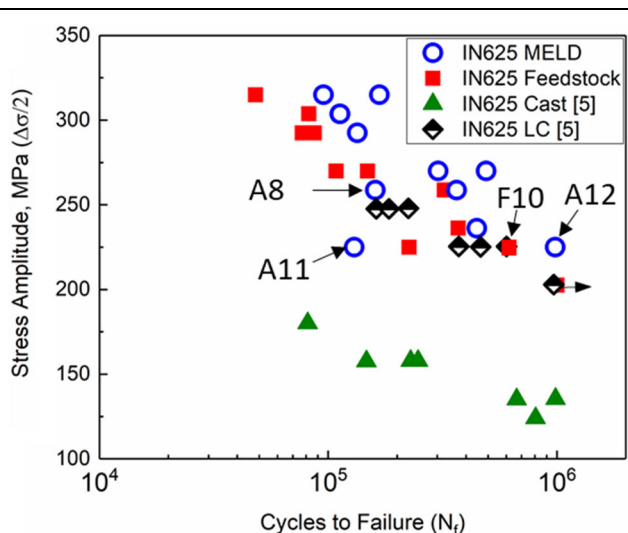


Fig. 5. Stress-life fatigue results comparing as-deposited IN625 to the feedstock, cast, and laser consolidation materials.⁵

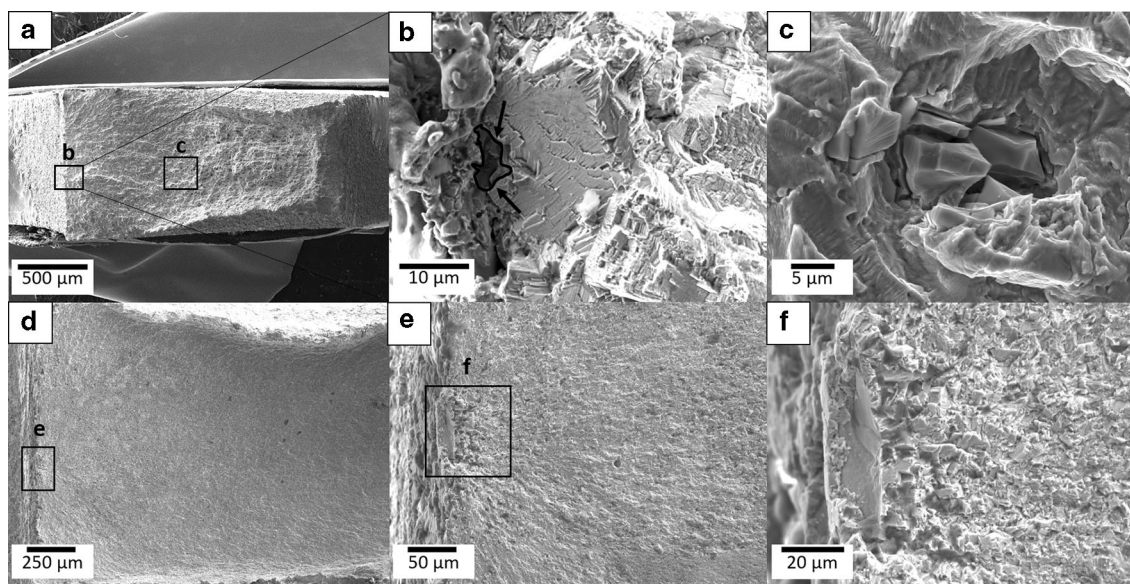


Fig. 6. (a) Fracture surface of the feedstock Specimen F10. (b) Magnified view of the fractured particle that initiated the fatigue crack. (c) Example of an intermetallic imbedded within microstructure. (d) Fracture surface of as-deposited Specimen A12. (e) Magnified view of the crack growth region. (f) Magnified view of the crack initiation site.

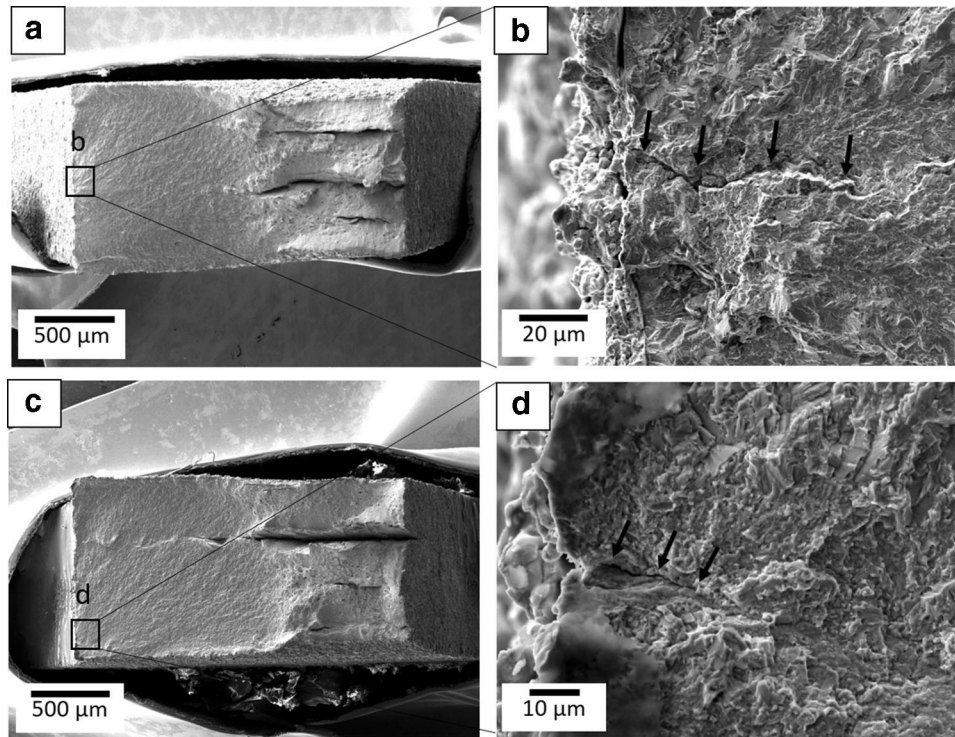


Fig. 7. (a) Macroscale view of the fracture surface of the as-deposited IN625 Specimen A11 and (b) magnified view of the delaminated layer interface that initiated the fatigue crack. (c) Macroscale fracture surface of as-deposited IN625 Specimen A8 and (d) magnified view of the delaminated layer interface that initiated the fatigue crack.

length is approximately $1600\ \mu\text{m}$. The refinement of the microstructure of as-deposited IN625 improved the crack growth resistance of the MSC regime and shifted the non-linear growth and increased overall crack length of the MELD fatigue specimen.

Figure 8b shows the comparison of the MSF model of total-life estimations along with the corresponding incubation life for both the feedstock and as-deposited IN625. Shown in Fig. 8b, the as-deposited IN625 experimental fatigue data exhibit a higher fatigue damage resistance and higher number of cycles to incubate a crack compared with the feedstock. The MSF mean model predictions, exhibited in Fig. 8b, for the feedstock and as-deposited IN625 were generated using the unique microstructural and mechanical characteristics of the corresponding material to capture the difference in observed fatigue behavior. The mean MSF model predictions were calculated using mean particle diameters and grain size for the feedstock of $10\ \mu\text{m}$ and $30\ \mu\text{m}$, respectively. In addition, the as-deposited IN625 mean model correlation was calculated using mean inclusion diameters and grain sizes of $2.2\ \mu\text{m}$ and $1\ \mu\text{m}$, respectively. We note that the MSF model correlated well with mean fatigue life results of both the feedstock and as-deposited IN625 while only varying the microstructure and mechanical strength parameters. Through the use of the MSF model, we note that the increase in fatigue life of as-deposited IN625 can be attributed in part to the decrease in particle and grain sizes.

Conversely, an increase in the particle and grain size results in reduced fatigue resistance. In addition, we note that the MSF model provided an estimation of the incubation life, where, as shown in Fig. 8b, a majority of the number of cycles to failure is dominated by the INC stage for the high cycle regime, whereas, for the low cycle regime, the MSC stage represents a larger fraction of the number of cycles to failure.

In addition to predicting the mean fatigue behavior, the MSF model can elucidate the role of microstructural features on the variability of fatigue behavior. As such, this scatter in the experimental results is captured by the MSF model through the upper and lower bound prediction for both the feedstock and as-deposited IN625, as shown in Fig. 8c, d, respectively. The upper and lower bounds for the feedstock were calculated using minimum and maximum inclusion diameters of $6\ \mu\text{m}$ and $13\ \mu\text{m}$ and minimum and maximum grain sizes of $23\ \mu\text{m}$ and $42\ \mu\text{m}$, respectively, whereas, for as-deposited IN625, the upper and lower bounds were calculated using minimum and maximum particle diameters of $1.3\ \mu\text{m}$ and $3\ \mu\text{m}$ and grain sizes of $0.3\ \mu\text{m}$ and $1.5\ \mu\text{m}$, respectively. We note the upper and lower bounds for feedstock exhibited a good relation to fatigue results and generally bounded the scatter of the experimental results. Likewise, for the as-deposited IN625, the MSF model also generally captured the scatter of the experimental results. However, several of the

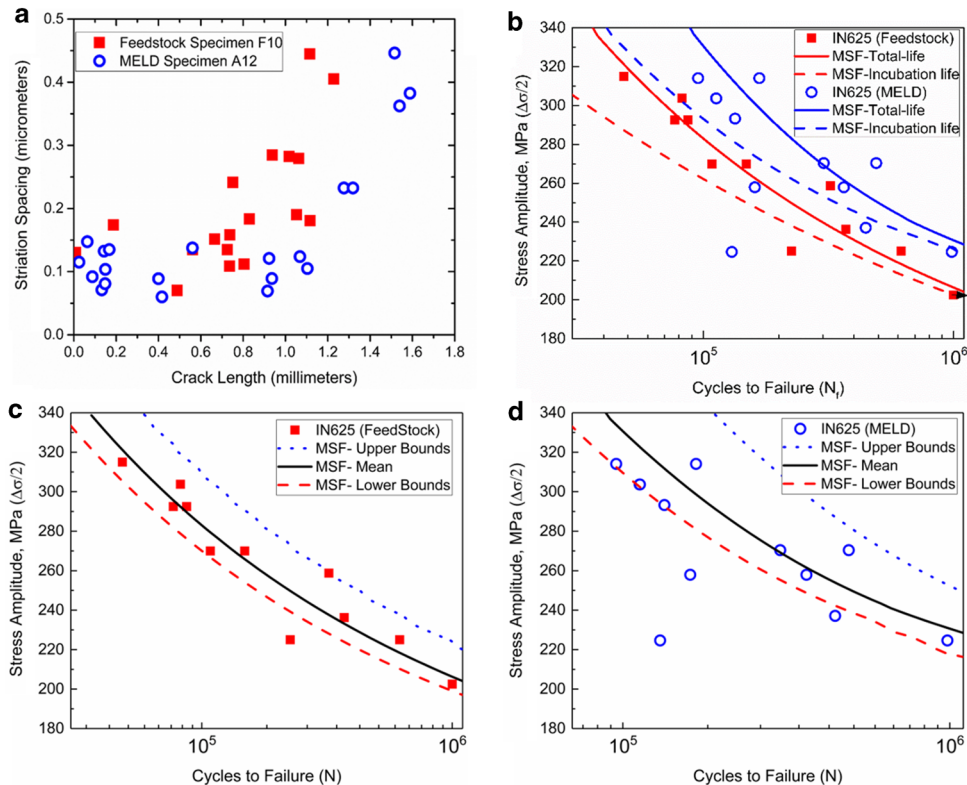


Fig. 8. (a) Striation spacing versus crack length for feedstock specimen F10 and MELD specimen A12. (b) Multi-stage fatigue (MSF) correlations of the mean fatigue life prediction, using mean particle diameter and grain size, of feedstock IN625 (red line) and MELD IN625 (blue line). (c) The MSF correlation to feedstock including upper and lower bounds. The upper and lower bounds for feedstock were determined using the minimum and maximum particle diameter and grain size, respectively. (d) The MSF correlation to as-deposited IN625 with upper and lower bounds. The upper and lower bounds for as-deposited IN625 were determined using the minimum and maximum particle diameter and grain size, respectively.

underperforming specimens were significantly outside the lower bounds of the MSF model prediction. However, this is not particularly surprising since the MSF model captures crack incubation from inclusion-like particles or voids, but has not been modified to account for interface delamination. Future efforts will be undertaken to address the adaption of the MSF model for prediction of crack incubation resulting from interface delamination.

CONCLUSION

The high-shear solid-state deposition process of the IN625 leads to dynamic recrystallization that refines the coarse granular microstructure of the feedstock into an equiaxed sub-micron microstructure as identified by TEM and EBSD. Additionally, this process breaks up the carbides into smaller and more uniformly distributed particles that promote improved fatigue resistance. TEM results of as-deposited IN625 revealed an ultra-refined microstructure compared with the feedstock. Fatigue results conducted in this study revealed that the as-deposited IN625 material exhibited improved fatigue properties compared with the feedstock. Post-mortem analysis revealed that the fatigue crack nucleation and crack growth mechanism for

a majority of as-deposited IN625 specimens was observed to behave similarly to the feedstock. However, for a few of the specimens, delamination of interface layers may have initiated fatigue cracks resulting in a lower number of cycles to failure. However, continued optimization of the MELD process will likely lead to more consistent fatigue behavior of the IN625 in the future. The fatigue crack growth results show that the high-shear deposited IN625 has a higher crack growth resistance compared with the feedstock. The physically small crack growth regime was altered because of the refined microstructure in which abundant grain boundaries, non-preferred crystallographic orientation, and refined carbides decreased the overall crack advancement per cycle in MELD IN625 specimens. Last, the MSF model correlated well with fatigue life results of the feedstock and as-deposited IN625, where the MSF fit was primarily a function of particle and grain size.

REFERENCES

1. L.E. Murr, E. Martinez, K.N. Amato, S.M. Gaytan, J. Hernandez, D.A. Ramirez, P.W. Shindo, F. Medina, and R.B. Wicker, *J. Mater. Res. Technol.* 1, 42 (2012).
2. L.E. Murr, S.M. Gaytan, D.A. Ramirez, E. Martinez, J. Hernandez, K.N. Amato, P.W. Shindo, F.R. Medina, and R.B. Wicker, *J. Mater. Sci. Technol.* 28, 1 (2012).

3. F.A. List, R.R. Dehoff, L.E. Lowe, and W.J. Sames, *Mater. Sci. Eng. A* 615, 191 (2014).
4. E. Brandl, U. Heckenberger, V. Holzinger, and D. Buchbinder, *Mater. Des.* 34, 159 (2012).
5. A. Theriault, L. Xue, and J.R. Dryden, *Mater. Sci. Eng. A* 516, 217 (2009).
6. M. Rombouts, G. Maes, M. Mertens, and W. Hendrix, *J. Laser Appl.* 24, 052007 (2012).
7. G.P. Dinda, A.K. Dasgupta, and J. Mazumder, *Mater. Sci. Eng. A* 509, 98 (2009).
8. J.J.S. Dilip, S. Babu, S.V. Rajan, K.H. Rafi, G.D.J. Ram, and B.E. Stucker, *Mater. Manuf. Process.* 28, 189 (2013).
9. S. Palanivel, P. Nelaturu, B. Glass, and R.S. Mishra, *Mater. Des.* 65, 934 (2015).
10. H. Hack, R. Link, E. Knudsen, B. Baker, and S. Olig, *Addit. Manuf.* 14, 105 (2017).
11. A. Mostafaei, Y. Behnamian, Y.L. Krimer, E.L. Stevens, J.L. Luo, and M. Chmielus, *Mater. Des.* 111, 482 (2016).
12. C.P. Paul, P. Ganesh, S.K. Mishra, P. Bhargava, J. Negi, and A.K. Nath, *Opt. Laser Technol.* 39, 800 (2007).
13. P. Ganesh, R. Kaul, C.P. Paul, P. Tiwari, S.K. Rai, R.C. Prasad, and L.M. Kukreja, *Mater. Sci. Eng. A* 527, 7490 (2010).
14. V. Shankar, K. Bhanu Sankara Rao, and S.L. Mannan, *J. Nucl. Mater.* 288, 222 (2001).
15. G. Aggen and C. Michael Allen, *ASM Handbook Volume I Properties and Selection: Irons, Steels, and High-Performance Alloys* (Materials Park: ASM International: The Materials Information Company, 2001).
16. H. Eiselstein and D. Tillack, *Var. Deriv.* 1 (1991).
17. L. Mataveli Suave, J. Cormier, D. Bertheau, P. Villechaise, A. Soula, Z. Hervier, and F. Hamon, *Mater. Sci. Eng. A* 650, 161 (2016).
18. O.G. Rivera, P.G. Allison, J.B. Jordon, O.L. Rodriguez, L.N. Brewer, Z. McClelland, W.R. Whittington, D. Francis, J. Su, R.L. Martens, and N. Hardwick, *Mater. Sci. Eng. A* 694, 1 (2017).
19. O.G. Rivera, P.G. Allison, L.N. Brewer, O.L. Rodriguez, J.B. Jordon, T. Liu, W.R. Whittington, R.L. Martens, Z. McClelland, C.J.T. Mason, L. Garcia, J.Q. Su, and N. Hardwick, *Mater. Sci. Eng. A* 724, 547 (2018).
20. L.H. Rettberg, J.B. Jordon, M.F. Horstemeyer, and J.W. Jones, *Metall. Mater. Trans. A Phys. Metall. Mater. Sci.* 43, 2260 (2012).
21. D.L. McDowell, *Int. J. Fatigue* 19, 127 (1998).
22. D.L. McDowell, *Eng. Fract. Mech.* 56, 357 (1997).
23. D.L. McDowell, K. Gall, M.F. Horstemeyer, and J. Fan, *Eng. Fract. Mech.* 70, 49 (2003).
24. R.R. McCullough, J.B. Jordon, A.T. Brammer, K. Manigandan, T.S. Srivatsan, P.G. Allison, and T.W. Rushing, *J. Mater. Eng. Perform.* 23, 65 (2014).
25. Y. Xue, D.L. McDowell, M.F. Horstemeyer, M.H. Dale, and J.B. Jordon, *Eng. Fract. Mech.* 74, 2810 (2007).
26. R.I. Rodriguez, J.B. Jordon, P.G. Allison, T. Rushing, and L. Garcia, *Mater. Sci. Eng. A* 654, 236 (2016).
27. Y. Xue, C.L. Burton, M.F. Horstemeyer, D.L. McDowell, and J.T. Berry, *Metall. Mater. Trans. B Process Metall. Mater. Process. Sci.* 38, 601 (2007).
28. M. Lugo, J.B. Jordon, J. Bernard, and M. Horstemeyer, *SAE Technical Papers* 2013-01-0980 (2013).
29. J.D. Bernard, J.B. Jordon, M.F. Horstemeyer, H.E. Kadiri, J. Baird, D. Lamb, and A.A. Luo, *Scr. Mater.* 63, 751 (2010).
30. J.B. Jordon, M.F. Horstemeyer, S.R. Daniewicz, H. Badarinarayan, and J. Grantham, *J. Eng. Mater. Technol.* 132, 041008 (2010).
31. J.B. Jordon and M.F. Horstemeyer, *J. Eng. Mater. Technol.* 136, 021004 (2014).
32. L.H. Rettberg, J.B. Jordon, M.F. Horstemeyer, and J.W. Jones, *A Trans.* 43, 2260 (2012).
33. M. Lugo, J.B. Jordon, K.N. Solanki, L.G. Hector, J.D. Bernard, A.A. Luo, and M.F. Horstemeyer, *Int. J. Fatigue* 52, 131 (2013).
34. J.B. Jordon, J.B. Gibson, and M.F. Horstemeyer, *Magnes. Technol.* 2011, 55 (2011).
35. P.G. Allison, Y. Hammi, J.B. Jordon, and M.F. Horstemeyer, *Powder Metall.* 56, 388 (2013).
36. Y. Xue, A. Pascu, M.F. Horstemeyer, L. Wang, and P.T. Wang, *Acta Mater.* 58, 4029 (2010).
37. Y. Xue, D.L. McDowell, M.F. Horstemeyer, M.H. Dale, and J.B. Jordon, *Eng. Fract. Mech.* 74, 2810 (2007).
38. J.M. Hughes, *The Application of Uncertainty Quantification (UQ) and Sensitivity Analysis (SA) Methodologies to Engineering Models and Mechanical Experiments* (Mississippi State University, 1985), pp. 553–558.
39. D.W. Brown, A. Jain, S.R. Agnew, and B. Clausen, *Mater. Sci. Forum* 539–543, 3407 (2007).
40. M. Kolbe, *Mater. Sci. Eng.* A319–321, 383 (2001).
41. J.H. Zhang, Z.Q. Hu, Y.B. Xu, and Z.G. Wang, *Metall. Trans. A* 23A (1992).